Contemporary Mathematics
http://ojs.wiserpub.com/index.php/CM/

Research Article

Hybrid PLM and ADRC Control for Sensorless Induction Motor Drive with Nine-Level Converter Employing SVPWM

Abdellah Oukassi*, Zakaria Boulghasoul, Lhoussain El Bahir

Systems Engineering and Applications Laboratory (LISA), National School of Applied Sciences (ENSA), Cadi Ayyad University, Marrakesh, Morocco
E-mail: abdououkassi16@gmail.com

Received: 28 May 2024; **Revised:** 19 July 2024; **Accepted:** 19 July 2024

Abstract: This paper outlines the design of a predictive controller combined with an active disturbance rejection control (ADRC)-type controller to enhance the dynamic performance of the induction motor powered by a nine-level converter. The predictive control law proposed is derived from the Poisson Laguerre model, based on predictive control. The motor is controlled using indirect field-oriented control, both with and without a speed sensor. For speed estimation, the Luenberger observer of order 4 is used. The predictive method utilized allows for the dynamic adjustment of control parameters based on those of the induction motor. The paper aims to eliminate internal and external disturbances and reduce total harmonic distortion (THD) through the use of a Nine-level cascaded H-bridge inverter. Space vector pulse width modulation (SVPWM) signals are generated using the logic of hexagon decomposition. The SVPWM method operates by decomposing higher-level hexagons into multiple two-level hexagons. The Poisson-Laguerre model (PLM) is also compared with the ADRC and the proportional-integral (PI) control. Simulations with MATLAB/SIMULINK software for an induction motor are performed to test the performance of each controller and the validity of the observer.

***Keywords*:** nine-level cascaded h-bridge inverter, SVPWM, induction machine, Luenberger observer, active disturbance rejection control (ADRC), Poisson-Laguerre model, indirect field oriented control (IFOC)

MSC: 93B53, 93C95

1. Introduction

Currently, several researchers are working on improving the dynamic behavior of electric machines used in electric vehicles. This research aims to minimize THD, adjust speed, and enhance torque ripple while considering internal and external disturbances. In this context, integrating advanced control techniques such as ADRC and PLM with multilevel converters into electric vehicle propulsion systems will enable automotive manufacturers to enhance vehicle reliability, energy efficiency, and overall performance. This approach will also meet increasing demands for driving comfort and reduced emissions. The induction motor is widely used in this field due to its robustness, cost-effectiveness, reliability, and efficiency. Induction motors exceed DC machines regarding speed variation, even though these machines are considered nonlinear, multivariable, and highly coupled systems [1, 2].

DOI: https://doi.org/10.37256/cm.5420245034

The decrease of the THD of the inverter's output voltages requires multi-level inverters. This will certainly contribute to the reduction of torque ripples as well. There are several multi-level UPS topologies. The difference lies in the switching mechanism and the number of voltage sources used at the input of multi-level inverters [3]. The three most commonly used and considered conventional topologies are the following: Multi-level inverters with looping diodes on neutral points (also known as neutral point clamped (NPC)), Floating capacitor multi-level inverters (also known as flying capacitor (FC)), and cascade h-bridge multi-level inverters (CH-BMI). This latter is selected for its ability to use several sources separately. In this paper, nine-level CH-BMI converters powered by DC batteries are used. Therefore, in the future, the proposed system may be powered by photovoltaic sources.

With the increase in voltage levels, we aim to achieve an output voltage waveform that closely resembles an ideal sinusoidal waveform. To accomplish this, the multilevel inverter must be controlled using pulse width modulation (PWM) or SVPWM techniques. Over the past three decades, numerous studies have been conducted for industrial applications [4]. The most widely used modulation techniques are sinusoidal pulse width modulation (SPWM) and space vector pulse width modulation (SVPWM). SPWM works by comparing a low-frequency sinusoidal wave with multiple high-frequency triangular carrier waves to generate control pulses [5, 6]. On the other hand, SVPWM reconstructs the reference voltage vector using the inverter's voltage vectors [7]. Each voltage vector corresponds to a specific combination of switching states in a three-phase voltage inverter. In this context, the SVPWM algorithmic approach is proposed. This approach has the advantage of minimizing THD and eliminating it.

Traditionally, most of the control systems are equipped with a sensor of speed connected to the rotor of the machine, which allows the determination of the rotational speed and in certain cases the position of the rotor. In certain industrial processes, the sensor of speed is either encumbering or too expensive. For these reasons, most current studies focus on enhancing the dynamic behavior of variable speed drives based on sensorless induction machines. The absence of the speed sensor implies the lack of this piece of information, which makes the task of algorithmic control more and more complicated. In this context, a model reference adaptive system (MRAS)-based velocity estimator was used in the document [8]. Luenberger state observers for estimating velocity are used [9, 10]. The results reveal the sensitivity of estimators and open-loop observers to variations in machine parameters. The Leunberger observer used in this work is a promising solution since it estimates real-time speed with the cancellation of external disturbances and supports unknown internal dynamics.

For a long time, proportional integrator-type controllers [11, 12] have been used for their simplicity, but the uncertainties of the induction motor model can make this control method inefficient in achieving the desired performance. Variations in engine parameters, due to factors such as temperature and external disturbances can compromise control accuracy. To ensure the required performance; special attention was paid to other types of control, namely the Active disturbance rejection control (ADRC) approach and adaptive predictive control. The authors [13] present the performance of an Active Disturbance Rejection Control for a five-stage H-Bridge inverter-powered induction motor using a PWM control. Adaptive-predictive control (APC) is an emerging and robust control technique against external disturbances. Based on the principle of predictive control of the induction machine, the controller has been developed by various methods to increase dynamic and static performance [14].

The aim of this control method [15] is to use prediction techniques to generate efficient commands for the multi-level inverter. This would enable achieving fast system dynamics while maintaining a feasible implementation in terms of computation. In the same context, the authors [16] highlight the interest in associating the model predictive control (MPC) command with multi-level converters. A Model-predictive direct power control of a three-phase three-level NPC PWM rectifier was also used [17]. This article focuses on the development of two tuning algorithms. The first is based on Poisson-Laguerre PLM models and the second is based on the ADRC model. The combination of two controls is also implemented for a sensor-less induction motor powered by a nine-level inverter.

In this paper, section 2 introduces the mathematical model of the induction motor (actuator), which includes equations describing the electrical and mechanical characteristics of the motor. Section 3 illustrates the nine-level converter with SVPWM control (pre-actuator). Section 4 illustrates the Luenberger estimator and the IFOC control. Section 5 describes the two PLM and ADRC controls; Section 6 illustrates the system block diagram. Section 7 reports the simulation results with analyses whereas the last section is devoted to providing some conclusions of the study.

2. Modelling of the actuator

In this paper, the chosen actuator is represented by an induction machine. Indeed, this machine is commonly used in electric vehicle propulsion systems due to its robustness, high energy efficiency, and ability to deliver high torque at low speed. The electrical modeling of this induction machine is generally represented in the reference frame $(d,\ q)$ (1). In this reference frame, the input vector consists of stator voltages, which facilitates the connection of the machine with the multi-level voltage inverter.

$$\begin{aligned} \frac{dx}{dt} &= [A][x] + [B][U] \\ [y] &= [C][x] \end{aligned} \tag{1}$$

With

$$[x]^t = [i_{sd}\ \ i_{sq}\ \ \phi_{rd}\ \ \phi_{rq}],\ \ [u]^t = [v_{sd}\ \ v_{sq}],$$

$$[A]^t = \begin{bmatrix} a_{11} & a_{12}\omega_s & a_{13} & a_{14}\omega_r \\ a_{21}\omega_s & a_{22} & a_{23}\omega_r & a_{24} \\ a_{31} & a_{32} & a_{33} & a_{34}\omega_g \\ a_{41} & a_{42} & a_{43}\omega_g & a_{44} \end{bmatrix}, \quad [B] = \begin{bmatrix} b_{11} & b_{12} \\ b_{21} & b_{22} \\ b_{31} & b_{32} \\ b_{41} & b_{42} \end{bmatrix},$$

$$a_{11} = a_{22} = -\left(\frac{1}{T_s\sigma} + \frac{1-\sigma}{T_r\sigma}\right),$$

$$a_{12} = -a_{21} = 1,\ a_{13} = a_{24} = \frac{1-\sigma}{T_r M\sigma},\ a_{14} = -a_{23} = \frac{1-\sigma}{\sigma M},\ a_{32} = a_{41} = 0,\ a_{33} = a_{44} = \frac{-1}{T_r},$$

$$a_{34} = -a_{43} = 1,\ b_{11} = b_{22} = \frac{1}{\sigma \cdot L_s},\ b_{31} = b_{32} = b_{41} = b_{42} = b_{12} = b_{21} = 0$$

The coefficients that are susceptible to variations due to changes in machine parameters (stator resistance and rotor resistance) are denoted $a_{11}, a_{13}, a_{42}, a_{44}$. The matrix can be represented as given in equation (2):

$$[A'] = [A] + [\Delta A] \tag{2}$$

With

$$[\Delta A] = \begin{bmatrix} \Delta a_{11} & 0 & \Delta a_{13} & 0 \\ 0 & \Delta a_{22} & 0 & \Delta a_{24} \\ \Delta a_{31} & 0 & \Delta a_{33} & 0 \\ 0 & \Delta a_{42} & 0 & \Delta a_{44} \end{bmatrix} \Delta a_{11} = \Delta a_{22} = -\left(\frac{K_{rs}}{T_s\sigma} + K_{rr}\frac{1-\sigma}{T_r\sigma}\right),$$

$$\Delta a_{13} = \Delta a_{24} = K_{rr}\frac{1-\sigma}{T_r M\sigma},\ \Delta a_{31} = \Delta a_{42} = K_{rr}\frac{M}{T_r}\Delta a_{31} = \Delta a_{42} = K_{rr}\frac{M}{T_r},\ \Delta a_{33} = \Delta a_{44} = K_{rr}\frac{-1}{T_r},$$

$0 \leq K_{rs}\% \leq 100,\ 0 \leq K_{rr}\% \leq 100$. K_{rr} and K_{rs} are the coefficients of resistance variation.

3. Pre-actuator modeling with its PWM control

3.1 *Pre-actuator modeling*

The topology of the cascaded H-bridge (CHB) converter used in this article is depicted in Figure 1. It converts DC signals into AC signals with very low harmonic distortion rates. Therefore, this topology is used to power the actuator mentioned in section 2. Several recent patents have been filed for this topology [18, 19]. The converter consists of a series of 12 single-phase bridges to supply power to a three-phase induction machine. Each phase contains 4 single-phase bridges. Each bridge can switch between, $+V_{dci}(Volts)$ 0, $-V_{dci}(Volts)$. This topology is suitable for connecting a renewable energy source such as photovoltaic modules to alternating current motors, especially by integrating fault management and optimization of the PV modules [20].

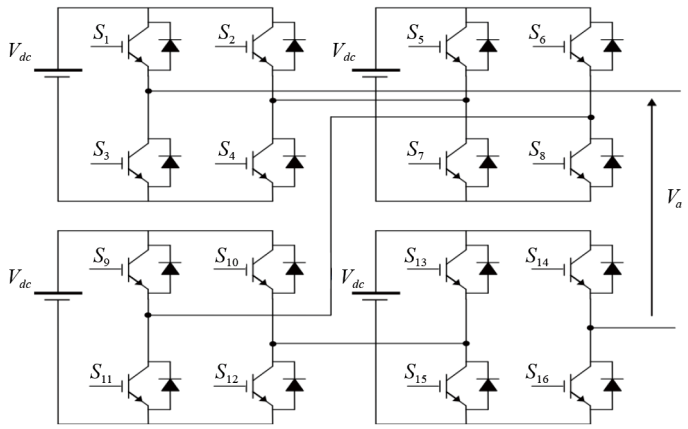

Figure 1. Converter structure (Nine CHB) for a single phase

3.2 *SVPWM control*

Several control techniques have been used to manage the switching operations of the CHB converter mentioned in section (3.1). It sounds like these methods are aimed at simplifying the computational complexity involved in space vector pulse width modulation (SVPWM) techniques. By breaking down higher-level hexagons into fundamental two-level hexagons, the mathematical computations become more manageable. This decomposition approach appears to be a common strategy across different references, each with its own specific breakdown and transformation process. In the first example from reference [21], a five-level space vector hexagon is broken down into six three-level hexagons, and then each three-level hexagon is further reduced to six two-level hexagons. This process likely simplifies the calculations involved in generating pulse width modulation signals for the inverter. Similarly, in the second example from reference [22], a seven-level SVPWM is decomposed into six four-level hexagons, and then each four-level hexagon is transformed into a two-level hexagon.

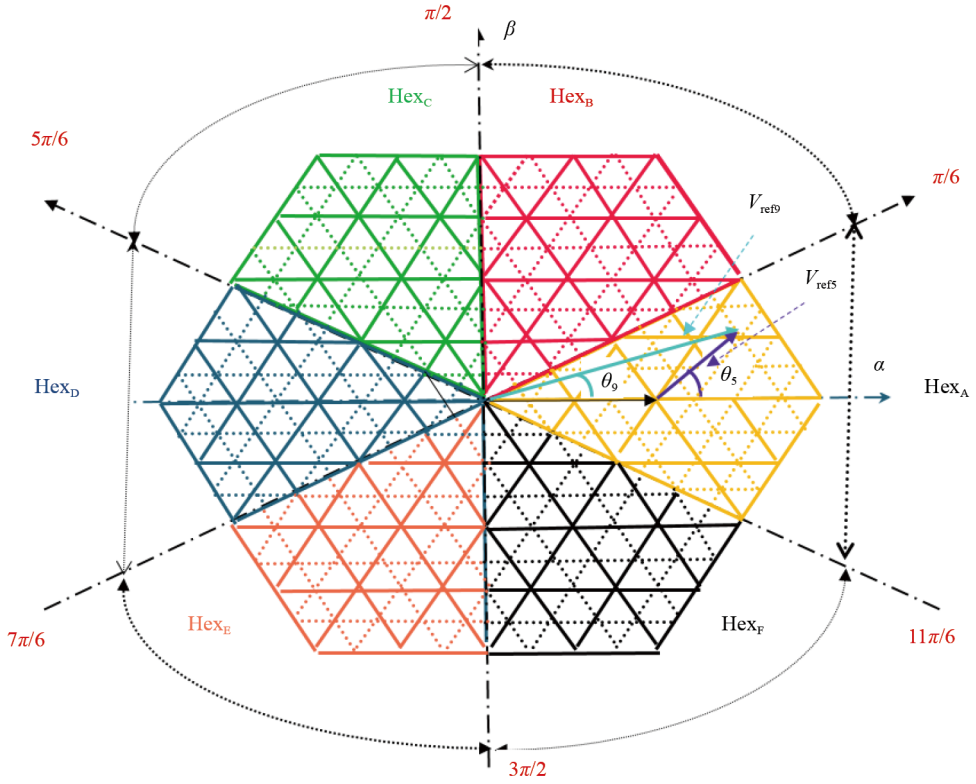

Figure 2. Resolution of nine-level SVD into five-level hexagons

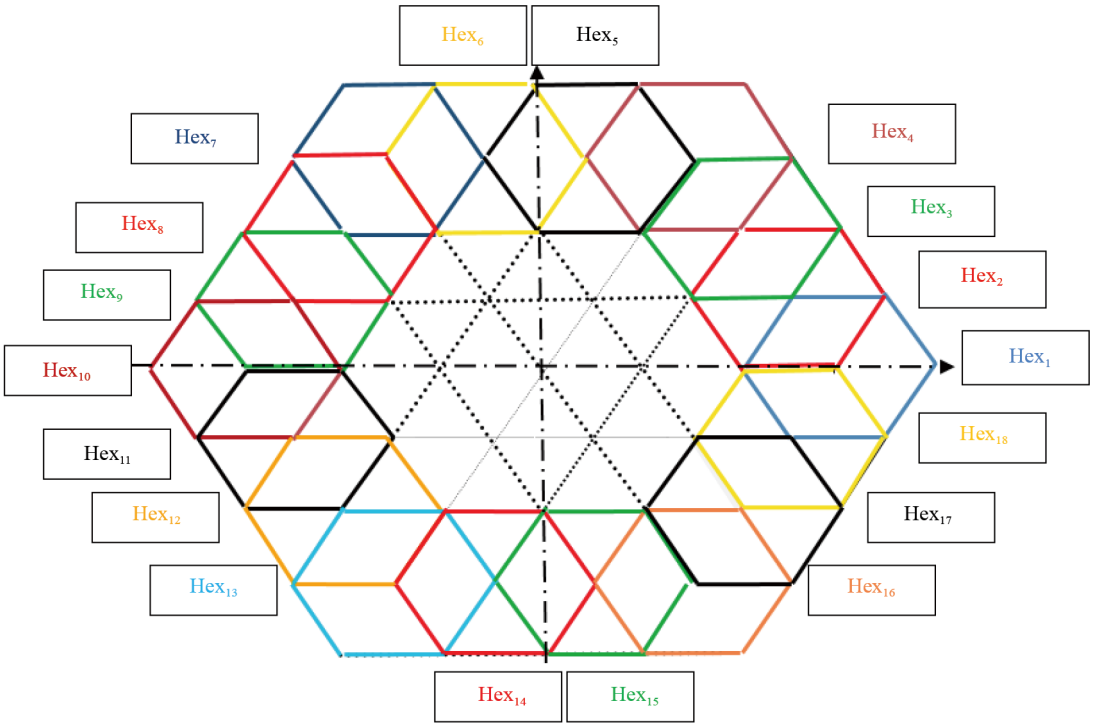

Figure 3. Resolution of five-level SVD into two-level hexagons

Based on this reasoning, the nine-level DVS is depicted in Figure 2. Initially, it is compressed into six hexagons, each consisting of five levels [7]. In total, to transition from level 9 to level 2, you would require 18 hexagons (Figure 3). It is indeed feasible to design a control algorithm (SVPWM) for an N-level converter. For an N-level space vector diagram, it comprises $(N-1)$ layers and $(N-1)^3$ triangles. Consequently, for a 9-level converter, it encompasses $9^3 = 729$ switching instants. Out of these 729 switching instances, 217 are independent, while the remaining 512 are redundant. The space vector diagram consists of 8 layers and 512 triangles.

$V_{(5\alpha)}$, $V_{(5\beta)}$ respectively $V_{(9\alpha)}$, $V_{(9\beta)}$ denote the components of the real (α) and imaginary (β) axis of $V_{(\text{ref5})}$ respectively $V_{(\text{ref9})}$.

Table 1. Mapping of $V_{(\text{ref2})}$ from $V_{(\text{ref5})}$ and mapping of $V_{(\text{ref5})}$ from $V_{(\text{ref9})}$

Mapping of $V_{(\text{ref2})}$ from $V_{(\text{ref5})}$ and 1.9 =< Coefficient k_1, k_2 <=3.5 (Part 1)				Mapping of $V_{(\text{ref5})}$ from $V_{(\text{ref9})}$ and 3.5=< K_3 <= 4 (Part 2)			
H	Voltage $V_{\alpha(2)}$	Voltage $V_{\beta(2)}$	θ (rad)	H	Voltage $V_{\alpha(5)}$	Voltage $V_{\beta(5)}$	θ (rad)
1	$V_{\alpha(5)} - (k_1 \cdot V_{dc})$	$V_{\beta(5)}$	[345 15]	A	$V_{\alpha(9)} - (V_{dc})$	$V_{\beta(9)}$	[11π/6 π/6]
2	$V_{\alpha(5)} - (k_2 \cdot V_{dc}$ cos(π/9))	$V_{\alpha(5)} - (k_2 \cdot V_{dc}$ sin(π/9))	[π/12 π/6]	B	$V_{\alpha(9)} - (K_3 \cdot V_{dc}$ cos(π/3))	$V_{\alpha(9)} - (K_3 \cdot V_{dc}$ sin(π/3))	[π/6 π/2]
3	$V_{\alpha(5)} - (k_2 \cdot V_{dc}$ cos(2π/9))	$V_{\alpha(5)} - (k_2 \cdot V_{dc}$ sin(2π/9))	[π/6 π/4]	C	$V_{\alpha(9)} - (K_3 \cdot V_{dc}$ cos(2π/3))	$V_{\alpha(9)} - (K_3 \cdot V_{dc}$ sin(2π/3))	[π/2 5π/6]
4	$V_{\alpha(5)} - (k_1 \cdot V_{dc}$ cos(π/3))	$V_{\alpha(5)} - (3V_{dc}$ sin(π/3))	[π/4 5π/12]	D	$V_{\alpha(9)} + (K_3 \cdot V_{dc})$	$V_{\alpha(9)} - (K_3 \cdot V_{dc})$	[5π/6 7π/6]
5	$V_{\alpha(5)} - (k_2 \cdot V_{dc}$ cos(4π/9))	$V_{\alpha(5)} - (k_2 \cdot V_{dc}$ sin(4π/9))	[5π/12 π/2]	E	$V_{\alpha(9)} - (K_3 \cdot V_{dc}$ cos(4π/3))	$V_{\alpha(9)} - (K_3 \cdot V_{dc}$ sin(4π/3))	[7π/6 π/2]
6	$V_{\alpha(5)} - (k_2 \cdot V_{dc}$ cos(5π/9))	$V_{\alpha(5)} - (k_2 \cdot V_{dc}$ sin(5π/9))	[π/2 7π/12]	F	$V_{\alpha(9)} - (K_3 \cdot V_{dc}$ cos(5π/3))	$V_{\alpha(9)} - (K_3 \cdot V_{dc}$ sin(5π/3))	[3π/2 1π/6]
7	$V_{\alpha(5)} - (k_1 \cdot V_{dc}$ cos(2π/3))	$V_{\alpha(5)} - (3V_{dc}$ sin(2π/3))	[7π/12 3π/4]				
8	$V_{\alpha(5)} - (k_2 \cdot V_{dc}$ cos(7π/9))	$V_{\alpha(5)} - (k_2 \cdot V_{dc}$ sin(7π/9))	[3π/4 5π/6]				
9	$V_{\alpha(5)} - (k_2 \cdot V_{dc}$ cos(8π/9))	$V_{\alpha(5)} - (k_2 \cdot V_{dc}$ sin(8π/9))	[5π/6 11π/12]				
10	$V_{\alpha(5)} + (k_1 \cdot V_{dc})$	$V_{\alpha(5)}$	[11π/12 13π/12]				
11	$V_{\alpha(5)} - (k_2 \cdot V_{dc}$ cos(10π/9))	$V_{\alpha(5)} - (k_2 \cdot V_{dc}$ sin(10π/9))	[13π/12 7π/6]				
12	$V_{\alpha(5)} - (k_2 \cdot V_{dc}$ cos(11π/9))	$V_{\alpha(5)} - (k_2 \cdot V_{dc}$ sin(11π/9))	[7π/6 15π/12]				
13	$V_{\alpha(5)}(k_1 \cdot V_{dc}$ cos(4π/3))	$V_{\alpha(5)} - (k_1 \cdot V_{dc}$ sin(4π/3))	[15π/12 17π/12]				
14	$V_{\alpha(5)} - (k_2 \cdot V_{dc}$ cos(13π/9))	$V_{\alpha(5)} - (k_2 \cdot V_{dc}$ sin(13π/9))	[17π/12 3π/2]				
15	$V_{\alpha(5)} - (k_2 \cdot V_{dc}$ cos(14π/9))	$V_{\alpha(5)} - (k_2 \cdot V_{dc}$ sin(14π/9))	[3π/2 19π/12]				
16	$V_{\alpha(5)} - (k_1 \cdot V_{dc}$ cos(5π/3))	$V_{\alpha(5)}(k_1 \cdot V_{dc}$ sin(5π/3))	[19π/12 21π/12]				
17	$V_{\alpha(5)} - (k_2 \cdot V_{dc}$ cos(16π/9))	$V_{\alpha(5)} - (k_2 \cdot V_{dc}$ sin(16π/9))	[21π/12 11π/6]				
18	$V_{\alpha(5)} - (k_2 \cdot V_{dc}$ cos(17π/9))	$V_{\alpha(5)} - (k_2 \cdot V_{dc}$ sin(17π/9))	[11π/6 23π/12]				

The principle of the algorithm involves establishing the relationships between the voltages in the $(\alpha,\ \beta)$ frame while transitioning from the 9-level inverter to the 5-level inverter. Then, finding the relationships, still within the same $(\alpha,\ \beta)$ frame, between the 5-level inverter and the 2-level inverter. Finally, positioning the angle θ within the appropriate

range. Table 1 enables the assembly of expressions for different voltages, facilitating transitions between levels (9 -5 - 2). Additionally, it provides the values of the angle position θ for each transition. In the proposed algorithm, the values of the coefficients K_1, K_2 and K_3 were well-chosen after several simulation tests. The correct choice of these coefficients increases the number of pulses for each voltage level (V_{dc}, 2 V_{dc}, 3 V_{dc}, and 4 V_{dc}).

4. Development of the observer of Luenberger and IFOC control

4.1 *Expressions of the observability matrix gains*

In the absence of a speed sensor, a deterministic machine observation model to reconstruct the rotation speed is developed. For this purpose, a state observer called a Luenberger observer is used. The determination of the observability coefficients requires the modeling of the induction machine in the mark (α, β). Referring to [23, 24], the estimated state model is given by equation (3):

$$\begin{aligned} \frac{d[\hat{x}]}{dt} &= [\hat{A}][\hat{x}(k)] + [B][U] + [K_{obs}]\,[\varepsilon] \\ [\hat{y}] &= [\hat{C}][\hat{x}] \\ [\varepsilon] &= [y] - [\hat{y}] \end{aligned} \tag{3}$$

With

$$[\hat{A}] = \begin{bmatrix} a_{11} & 0 & a_{13} & a_{14}\cdot\widehat{\omega}_r \\ 0 & a_{22} & a_{23}\cdot\widehat{\omega}_r & a_{24} \\ a_{31} & a_{32} & a_{33} & -a_{34}\cdot\widehat{\omega}_r \\ a_{41} & a_{42} & -a_{43}\cdot\widehat{\omega}_r & a_{44} \end{bmatrix},\ [B] = \begin{bmatrix} b_{11} & b_{12} \\ b_{21} & b_{22} \\ b_{31} & b_{32} \\ b_{41} & b_{42} \end{bmatrix} \text{ and } [C] = \begin{bmatrix} 1 & 0 & 0 & 0 \\ 0 & 1 & 0 & 0 \end{bmatrix}$$

$$\hat{x}^t = \left[\hat{i}_{s\alpha},\ \hat{i}_{s\beta},\ \hat{\varphi}_{r\alpha},\ \hat{\varphi}_{r\beta}\right],\ \hat{y}^t = \left[\hat{i}_{s\alpha},\ \hat{i}_{s\beta}\right] \text{ and } [K_{obs}] = \begin{bmatrix} k_{11} & k_{12} & k_{13} & k_{14} \\ k_{21} & k_{22} & k_{23} & k_{24} \end{bmatrix}$$

From the state matrix, it is noticed that the system has several symmetries. This will directly influence the observation matrix, which must also have symmetries [25]. Therefore, we can write:

$$k_{11} = k_{22},\ k_{13} = k_{24},\ k_{12} = -k_{21},\ k_{14} = -k_{23}$$

We consider a system of order n, whose equations are given by (1): In this case, the system is said to be completely observable if there is a moment $t_1 \geq t_0$, such that the knowledge of the input $[U(t_0, t_1)]$ and the knowledge of the output $[Y(t_0, t_1)]$ for all values is sufficient to determine the initial state $[x(t_0)] = [x_0]$. The observability criterion is that the dimension matrix $(n, m \times n)$ known as the observability matrix is of maximum rank (or rank = n). This matrix is given by equation (4):

$$[W_{obs}] = \begin{bmatrix} C \\ C \cdot A \\ C \cdot A^2 \\ \cdots \\ C \cdot A^{n-1} \end{bmatrix} \tag{4}$$

The dynamics of the observer depend on the matrix $[A'd]$ and its values which are the roots of (5): $[S \cdot I - A'd]$ with:

$$[A'd] = [A] - [K_{\text{obs}}][C] \tag{5}$$

The expressions of the observability matrix gains are given by equations (6-9)

$$k_{11} = (k-1)\left(\frac{1}{\sigma}\left(\frac{1}{T_s} + \frac{(1-\sigma)R_r}{L_r}\right) + \frac{R_r}{L_r}\right) \tag{6}$$

$$k_{12} = (1-k)\omega_r \tag{7}$$

$$k_{13} = \left(1-k^2\right)\left(\frac{MR_r}{L_r} - \frac{L_s L_r}{M}\left(\frac{1}{T_s} + \frac{(1-\sigma)R_r}{L_r}\right)\right) + \frac{L_s L_r (1-k)}{M}\left(\frac{1}{\sigma}\left(\frac{1}{T_s} + \frac{(1-\sigma)R_r}{L_r}\right) + \frac{R_r}{L_r}\right) \tag{8}$$

$$k_{14} = \frac{\sigma L_s L_r \omega_r (1-k)}{M} \tag{9}$$

4.2 *Expressions of the observability matrix gains*

To enhance the accuracy of estimation, many researchers have suggested the utilization of a PI-type adaptation mechanism. This approach aims to refine the estimation process and improve overall accuracy. To determine the coefficients of adapter P and I, minimizing the estimation error ($[e(k)] = [x(k)] - [\hat{x}(k)]$) as much as possible between the actual and the estimated state vectors is sufficient. The Lyapunov function is used in the stability theory of dynamic systems [26, 27]. The expression of this function is given by equation (10).

$$V = (x-\hat{x})(x-\hat{x})^T + \frac{(\omega_r - \hat{\omega}_r)^2}{\rho} \tag{10}$$

Where: ρ stands for a positive constant coefficient, while $(x-\hat{x})$ symbolizes the estimation error vector. The derivative of V in time, which should be negative, is defined by (11) the following equation:

$$\frac{dV}{dt} = \frac{d(x-\hat{x})}{dt}(x-\hat{x})^T + \frac{d(x-\hat{x})^T}{dt}(x-\hat{x}) + \frac{1}{\rho}\frac{d(\omega_r - \hat{\omega}_r)^2}{dt} \tag{11}$$

Equation (11) can be expanded to obtain equation (12). The latter can be further expanded to obtain equation (13).

$$\frac{dV}{dt} = \frac{d(x-\hat{x})}{dt}(x-\hat{x})^T + \frac{d(x-\hat{x})^T}{dt}(x-\hat{x}) + \frac{1}{\rho}\frac{d(\omega_r-\hat{\omega}_r)^2}{dt} \tag{12}$$

$$\begin{aligned}\frac{dV}{dt} = & \left[(B-AK)^T + (B-AK)\right](x-\hat{x})^T(x-\hat{x}) \\ & + 2(\omega_r-\hat{\omega}_r)\frac{\sigma L_s L_r}{M}(1-k)\left(\hat{\varphi}_{r\beta}\left(i_{s\alpha}-\hat{i}_{s\alpha}\right) - \hat{\varphi}_{r\alpha}\left(i_{s\beta}-\hat{i}_{s\beta}\right)\right) \\ & - \frac{2(\omega_r-\hat{\omega}_r)}{\rho}\frac{d\hat{\omega}_r}{dt}\end{aligned} \tag{13}$$

The expression $\left[(B-AK)^T + (B-AK)\right](x-\hat{x})^T(x-\hat{x})$ is always negative. Both last terms may be set to zero since (14) they are insignificant in comparison with the first.

$$2(\omega_r-\hat{\omega}_r)\frac{\sigma L_s L_r}{M}(1-k)\left(\hat{\varphi}_{r\beta}\left(i_{s\alpha}-\hat{i}_{s\alpha}\right) - \hat{\varphi}_{r\alpha}\left(i_{s\beta}-\hat{i}_{s\beta}\right)\right) - \frac{2(\omega_r-\hat{\omega}_r)}{\rho}\frac{d\hat{\omega}_r}{dt} = 0 \tag{14}$$

Thus, the expression of $\hat{\omega}_r$ becomes (15):

$$\hat{\omega}_r = \rho\frac{\sigma L_s L_r}{M}(1-k)\int\left(\hat{\varphi}_{r\beta}\left(i_{s\alpha}-\hat{i}_{s\alpha}\right) - \hat{\varphi}_{r\alpha}\left(i_{s\beta}-\hat{i}_{s\beta}\right)\right)dt \tag{15}$$

Many scientists have suggested an adaptation mechanism for PI to improve the accuracy of estimates. The following expression (16) gives that of the estimated speed:

$$\hat{\omega}_r = \left(K_p + \frac{K_i}{s}\right)\left(\hat{\varphi}_{r\beta}\left(i_{s\alpha}-\hat{i}_{s\alpha}\right) - \hat{\varphi}_{r\alpha}\left(i_{s\beta}-\hat{i}_{s\beta}\right)\right) \tag{16}$$

Where: K_p and K_i are positive constants (17).

$$\hat{\omega}_r = \left(K_{p\omega r} + \frac{K_{i\omega r}}{s}\right)\cdot e_{\omega r} \tag{17}$$

With

$$e^t = \left[i_{s\alpha}-\hat{i}_{s\alpha},\ i_{s\beta}-\hat{i}_{s\beta},\ \varphi_{r\alpha}-\hat{\varphi}_{r\alpha},\ \varphi_{r\beta}-\hat{\varphi}_{r\beta}\right], \quad \text{and} \quad e_{\omega r} = \left[\left(i_{\alpha s}-\hat{i}_{\alpha s}\right)\hat{\varphi}_{r\beta} - \left(i_{\beta s}-\hat{i}_{\beta s}\right)\hat{\varphi}_{r\alpha}\right]$$

Just fine-tune the gains K_p and K_i to get an estimated speed similar to the actual rotation speed.

4.3 *Indirect field-oriented control approach*

The direct state model obtained in Section 2 for designing speed controllers based on induction machines is very challenging, if not impossible. Therefore, researchers use models that resemble those of a DC machine. Currently, the IFOC approach is widely used in speed variation devices by induction machines. This gives a model that resembles that of a DC machine. In this architecture, flux and torque are decoupled and controlled separately. The estimated angular frequency (obtained from Luenberger Observer) is given below (18), based on references [24, 28].

$$\hat{\omega}_s = \hat{\omega}_r + \hat{\omega}_g \tag{18}$$

The space angle $\hat{\theta}_s$ can be written as given in equation (19):

$$\hat{\theta}_s = \int \hat{\omega}_s dt \tag{19}$$

The asynchronous machine equations used in the control circuit are given by equations (20) and (21):

$$0 = R_r i_{rd} + \frac{d\varphi_{rd}}{dt} - \omega_g \varphi_{rq} \tag{20}$$

$$0 = R_r i_{rd} + \frac{d\varphi_{rq}}{dt} + \omega_g \varphi_{rd} \tag{21}$$

For decoupling control, we have $\varphi_{rq} = 0,\ \varphi_{rd} = \varphi_r$ The expressions of the sliding pulsation $\hat{\omega}_g$ and the torque C_e are given by (22) and (23):

$$\hat{\omega}_g = \frac{i_{sq}}{i_\varphi L_r} \hat{R}_r \tag{22}$$

$$C_e = p \frac{M^2}{L_r} i_\varphi i_{sq} \tag{23}$$

The mechanical speed estimated as a function of electromagnetic torque and load torque is given by the following expression (24):

$$J \frac{d\hat{\Omega}_r}{dt} = -K_f \hat{\Omega}_r + (C_e - C_r) \tag{24}$$

By introducing the concept of decoupling and based on the IFOC structure, the following expressions can be used (25):

$$\begin{aligned} \hat{V}_{sdref} &= v_{sd}^{*} - \hat{e}_d \\ \hat{V}_{sqref} &= v_{sq}^{*} - \hat{e}_q \end{aligned} \tag{25}$$

Based on the principle of indirect decoupling [21], the reference voltages for the stator windings are given by equation (26).

$$\begin{cases} v_{sd}^{*} = \sigma Ls \dfrac{di_{sd}}{dt} + \sigma Ls \left(\dfrac{1}{T_s \cdot \sigma} + \dfrac{1-\sigma}{T_r \cdot \sigma} \right) i_{sd}^{*} \\ v_{sq}^{*} = \sigma Ls \dfrac{di_{sq}}{dt} + \sigma Ls \left(\dfrac{1}{T_s \cdot \sigma} + \dfrac{1-\sigma}{T_r \cdot \sigma} \right) i_{sq}^{*} \end{cases} \tag{26}$$

5. Predictive control and ADRC control

5.1 *Adjustment of coefficients using predictive control based on the Poisson-Laguerre model*

In systems control, it is always necessary to have an idea of the behavior and complexity of these systems. The information obtained based on the index or impulsive responses makes it possible to determine the dominant time constants and the resonance frequencies of the system to be controlled [29]. This information is very useful in determining the order of the system when establishing the model. Among the different representations of continuous linear systems, orthogonal series such as Legendre [30] and the Poisson-Laguerre models [29] indicate a high efficiency in the representation of well-damped systems. The application of this PLM model helps improve the response time of mechanical variables, specifically the mechanical rotation speed of the actuator. The purpose of this section is to describe the Poisson-Laguerre models used in the modelling of the vector-controlled induction machine. The classical Poisson-Laguerre impulse functions are defined by equation (27), referring to [31].

$$p_k(t,\ \lambda) = \frac{t^k e^{-\lambda t}}{k!},\ k = 1,\ 2,\ \ldots \tag{27}$$

With $\lambda\,(\text{réel}) > 0$.
The Laplace transform is given by (28):

$$\pi_k(s,\ \lambda) = \frac{1}{(s+\lambda)^k} \tag{28}$$

The following series represent these PLM models [29]. We, then, adopt the models given by the expression (29) for a transfer function $(G(s))$ between electromagnetic torque and mechanical speed.

$$G(s) = \sum_{i=1}^{n} g_i \pi_i (s+\lambda) = \sum_{i=1}^{n} g_i \frac{1}{(s+\lambda)^i} \tag{29}$$

Where: $\lambda > 0$ is the dominating pole of the system, $\{g_i\}$ are the PL parameters and (n) is the truncation order of the PL series.

The following state space representation is obtained (30):

$$\begin{aligned} \dot{x}^{PL}(t) &= A^{PL}x^{PL}(t) + B^{PL}u(t) \\ y(t) &= g^T x^{PL}(t) \end{aligned} \tag{30}$$

Where $g^T = [g_1 \ \dots \ g_n]$, $x^{PL}(t) = \left[x_1^{PL}(t) \ \dots \ x_n^{PL}(t)\right]^T$

$$A^{PL} = \begin{bmatrix} -\lambda & 0 & \cdots & \cdots & 0 \\ 1 & -\lambda & \ddots & & \vdots \\ 0 & \ddots & \ddots & \ddots & \vdots \\ \vdots & \ddots & \ddots & \ddots & 0 \\ 0 & \dots & 0 & 1 & -\lambda \end{bmatrix} \text{ and } B^{PL} = \begin{bmatrix} 1 \\ 0 \\ \vdots \\ 0 \end{bmatrix}$$

The control signal is denoted by $u(t)$, the state vector by $x^{PL}(t) = \left[x_1^{PL}(t) \ \dots \ x_n^{PL}(t)\right]^T$, and the output of the PL models by $y(t)$. These statements are derived as given in equation (31).

$$x_{i+1}^{PL}(t) = \frac{1}{(s+\lambda)} x_i^{PL}(t) = \frac{1}{(s+\lambda)^{i+1}} u(t), \ x_0^{PL}(t) = u(t) \tag{31}$$

The PLM requires knowledge of the dominant pole λ, of the system, and identification of the model parameters $\{g_i\}$. The optimal value of λ is determined by minimizing the criterion $J_g(\lambda)$ of equation (32), where y_k represents the measured output of the actual system and $\hat{g}x_k = \hat{y}_k$ is the estimated output by the PLM.

$$J_e(\lambda) = \sum_{k=1}^{N} |y_k - \hat{g}x_k| \tag{32}$$

The recursive least squares algorithm is used to identify unknown parameters ($\hat{g}$) of the PLM.

5.2 *Predictive control law (predictive control (APC) applied to motor using PLM)*

The objective of predictive control is to generate a control signal $u(t)$ that ensures the controlled variable $y(t)$ aligns with a desired reference value $r(t)$ over a specified future prediction horizon $T > 0$. This could be expressed by equation (33), referring to [32].

$$y(t+T) = r(t+T) \tag{33}$$

Based on the Maclaurin series, the output predictor $y(t+T)$ can be written as (34), referring to [32].

$$y(t+T) = y(t) + \sum_{i=1}^{+\infty} \frac{T^i}{i!} \frac{d^i}{dt^i} y(t) \tag{34}$$

Taking into account the Poisson-Laguerre model (PLM), equation (30), we will have the expression (35).

$$y(t+T) = y(t) + g^T M(T) x^{PL}(t) + K^T U(t) \tag{35}$$

With

$$M(T) = \sum_{i=1}^{+\infty} \frac{T^i}{i!} A^i = e^{AT} - I_n = e^{-\lambda T}\Gamma(T) - I;\ \Gamma(T) = \begin{bmatrix} 1 & 0 & \cdots & 0 \\ T & 1 & \ddots & \vdots \\ \vdots & \ddots & \ddots & 0 \\ \dfrac{T^{n-1}}{(n-1)!} & \cdots & T & 1 \end{bmatrix},$$

Where $K(T) = [k_1(T)\ k_2(T)\ \ldots]^T$

$$k_i(T) = g^T A^{-i} \left[e^{-\lambda T}\Gamma(T) - \sum_{j=1}^{i} \frac{(AT)^{j-1}}{(j-1)!} \right] B \ \text{ and } \ U(t) = \left[u(t)\ \frac{du(t)}{dt}\ \frac{d^2u(t)}{dt^2}\ \ldots \right]^T$$

Substitution of equation (33) in (35) leads to (36):

$$K^*(s)u(t) = [r(t+T) - y(t)] - g^T M(T) x^{PL}(T) \tag{36}$$

Where: The function $K^*(s)$, is written (37):

$$K^*(s) = \sum_{i=1}^{+\infty} k_i(T) s^{i-1} \tag{37}$$

The series (37) must be truncated in a well-defined order while applying the following constraint to the control signal. This constraint is given by equation (38).

$$\frac{d^i u(t)}{dt} = 0 \quad \forall i \geq N_u \tag{38}$$

The relation (38) implies that the higher-order derivatives are null. Therefore (36) can be written as (39):

$$K(s)u(t) = [r(t+T) - y(t)] - g^T M(T) x^{PL}(T) \tag{39}$$

In equation (39), we can extract the function $K(s)$ as written in equation (40):

$$K(s) = k_{Nu}(T)s^{Nu-1} + \ldots + k_2(T)s + k_1(T) \tag{40}$$

If we notice (41) that:

$$F(s) = \frac{1}{K(s)} \tag{41}$$

The control signal, which will be determined based on the stability of the function, is given (42):

$$u(t) = F(s)[r(t+T) - y(t)] - F(s)g^T M(T)x^{PL}(T) \tag{42}$$

To be stable, the following conditions must be met. Based on this inequality (43), we can derive these conditions.

$$\forall i = 1 \ \ldots \ N_u k_i(T) > 0 \tag{43}$$

The relation (42) can be described in the following manner:

- If $Nu = 1$. Then, this expression is a state feedback control.
- If $Nu > 1$. Then, this expression is a state feedback control. Based on the expression (42), the control signal takes the following form (44):

$$u(t) = F(s)[r(t+T) - y(t)] - F(s)C(s)u(t) \tag{44}$$

Where: The function $C(s)$, is written (45):

$$C(s) = \sum_{i=1}^{n} c_i(T)\frac{1}{(s+\lambda)^i} \tag{45}$$

And (46):

$$[c_1(T)\ c_2(T)\ \ldots\ c_n(T)] = c^T(T) = g^T M(T) \tag{46}$$

Figure 4 highlights the speed control of the induction machine using the predictive control based on the Poisson-Laguerre model [32].

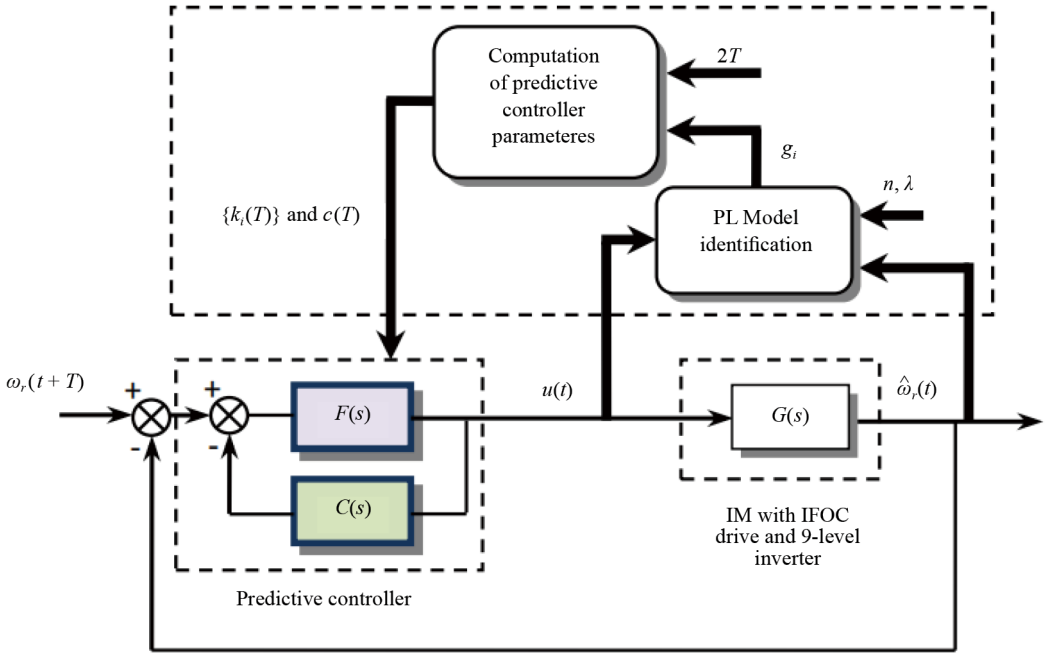

Figure 4. Predictive control (based on PLM) block diagram to control mechanical rotation speed

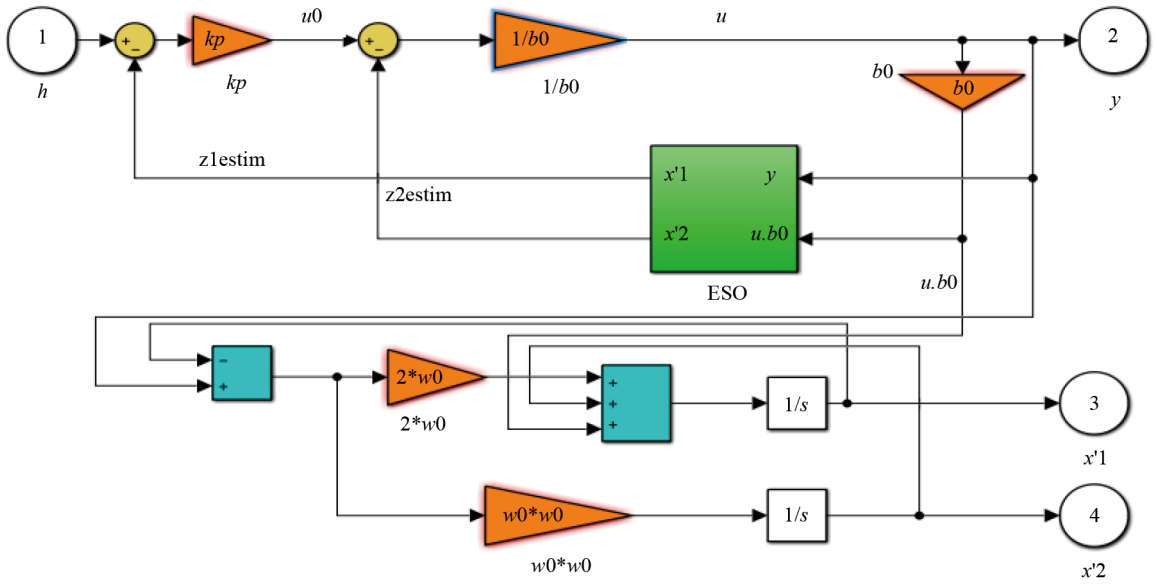

Figure 5. ADRC controller using ESO

5.3 *Active disturbance rejection controller*

Various internal disturbances, including rotor and stator resistance variations and external disruptions like load torque and speed fluctuations, can impact machine performance, particularly noticeable at low speeds. Hence, employing active disturbance rejection control serves as a dependable control strategy. ADRC, stemming from proportional-integral

derivation (PID), is its cornerstone, relying on error-based control instead of a model [33, 34]. In this control, The Extended State Observer (ESO) is used (see Figure 5). Indeed, The ESO is a robust observer utilized in control systems to estimate both the system state and the disturbance state. This capability enables more precise control even in the presence of uncertainties and disturbances, with a fast response time. The main equation of an Active Disturbance Rejection Control (ADRC) controller is given by (47).

$$y = f(y,\ \varepsilon,\ t) + b_0 u \tag{47}$$

In this context: u denotes an input variable, y represents an output variable, $b0$ stands for a constant, and ε signifies the total of external and internal disturbances.

Expressing equation (47) using the state-space form yields (48):

$$\begin{cases} y = \begin{pmatrix} 1 \\ 0 \end{pmatrix}^T \cdot x \\ \\ \dot{x} = \begin{pmatrix} 0 & 1 \\ 0 & 0 \end{pmatrix} \cdot x + \begin{pmatrix} 1 \\ 0 \end{pmatrix} \cdot b_0 u + \begin{pmatrix} 0 \\ 1 \end{pmatrix} \cdot \dot{f} \end{cases} \tag{48}$$

The following equation expresses the Extended State Observer (49):

$$\begin{cases} \hat{y} = \begin{pmatrix} 1 \\ 0 \end{pmatrix}^T \cdot z \\ \\ \dot{z} = \begin{pmatrix} 0 & 1 \\ 0 & 0 \end{pmatrix} \cdot z + \begin{pmatrix} 1 \\ 0 \end{pmatrix} \cdot b_0 u + \begin{pmatrix} 2\omega_0 \\ \omega_0^2 \end{pmatrix} \cdot (y - \hat{y}) \end{cases} \tag{49}$$

With: ω_0 being the observer bandwidth, determined by pole placement, aiming to achieve a rapid and highquality output.

Following ADRC, a control law is then established by (50):

$$u = \frac{u_0 - z_2}{b_0} \tag{50}$$

Where z_2 stands as a precise estimation of "f", and as an accurate estimation of "y".

The resulting equation (47) becomes (51).

$$\begin{cases} u_0 = K_p\,(h - z_1) \\ \dot{y} = u_0 + (f - z_2) \approx u_0 \end{cases} \tag{51}$$

Where: h denotes the reference input signal.

Equation (24) can be converted to the canonical form ADRC. This gives the corresponding equation below (52).

$$\frac{d\Omega}{dt} = f_{\Omega}(\Omega,\ \varepsilon,\ t) + \frac{C_{em}(t)}{J} \tag{52}$$

Equations (26) above can be expressed in ADRC canonical form as the corresponding equations below (53), (54):

$$\frac{di_{sd}}{dt} = f_d\,(i_{sd},\ \varepsilon,\ t) + \frac{V_{sd}(t)}{L_s\sigma} \tag{53}$$

$$\frac{di_{sq}}{dt} = f_q\,(i_{sq},\ \varepsilon,\ t) + \frac{V_{sq}(t)}{L_s\sigma} \tag{54}$$

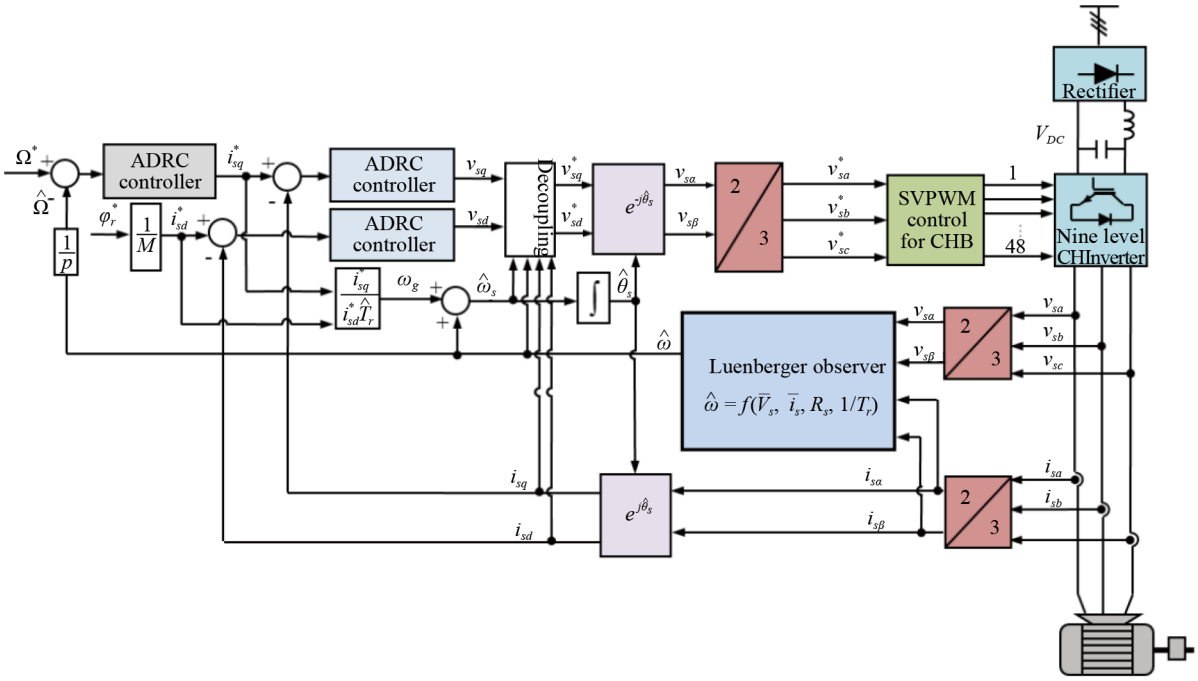

Figure 6. System proposed for a sensorless induction machine powered by a nine-level converter using three ADRC-type controls

6. Proposed system

In Figure 6, the proposed system is based on the ADRC command (ADRC for $Ce = f(\omega)$), ADRC control for $V_{sd} = f(I_{sd})$, and ADRC control for $V_{sq} = f(I_{sq})$). The block diagram not mentioned here contains only three IPs instead of three ADRCs. The control of the cascade converter switches is managed by an SVPWM. The proposed system block diagrams are illustrated in Figure 6 and Figure 7. In Figure 7, the combination between the PLM control is ADRC is used (PLM for $Ce = f(\omega)$, ADRC control for $V_{sd} = f(I_{sd})$, and ADRC control for $V_{sq} = f(i_{sq})$). In this figure, the mechanical speed is estimated using a state observer (Leunberger observer) and compared to the reference speed. Based on the model of Predictive Current Control (PLM), a reference electromagnetic torque is obtained. Subsequently, the principles of field-oriented control (FOC) are applied to determine the reference quadrature stator current i_{sq}. This control principle is also

used to derive a reference direct stator current i_{sd}. By combining the indirect method of field control with the principles of Active Disturbance Rejection Control (ADRC), reference voltages V_{sd} and V_{sq} are established. The inverse Park matrix is employed to derive the three reference voltages V_{sa}, V_{sb}, and V_{sc}. These waveforms are utilized in an algorithm to calculate and determine the switching times of the nine-level converter switches. This converter generates three voltages to supply the asynchronous machine stator. In closed-loop operation, sensors for the three stator voltages and three stator currents are used to reconstruct a state model of the machine. Using this observed model, the rotational speed is estimated. In Figure 6, the proposed system is based on the ADRC command (ADRC for $Ce = f(\omega)$), ADRC control for $V_{sd} = f(I_{sd})$, and ADRC control for $V_{sq} = f(I_{sq})$). The block diagram not mentioned here contains only three IPs instead of three ADRCs. The control of the cascade converter switches is managed by an SVPWM.

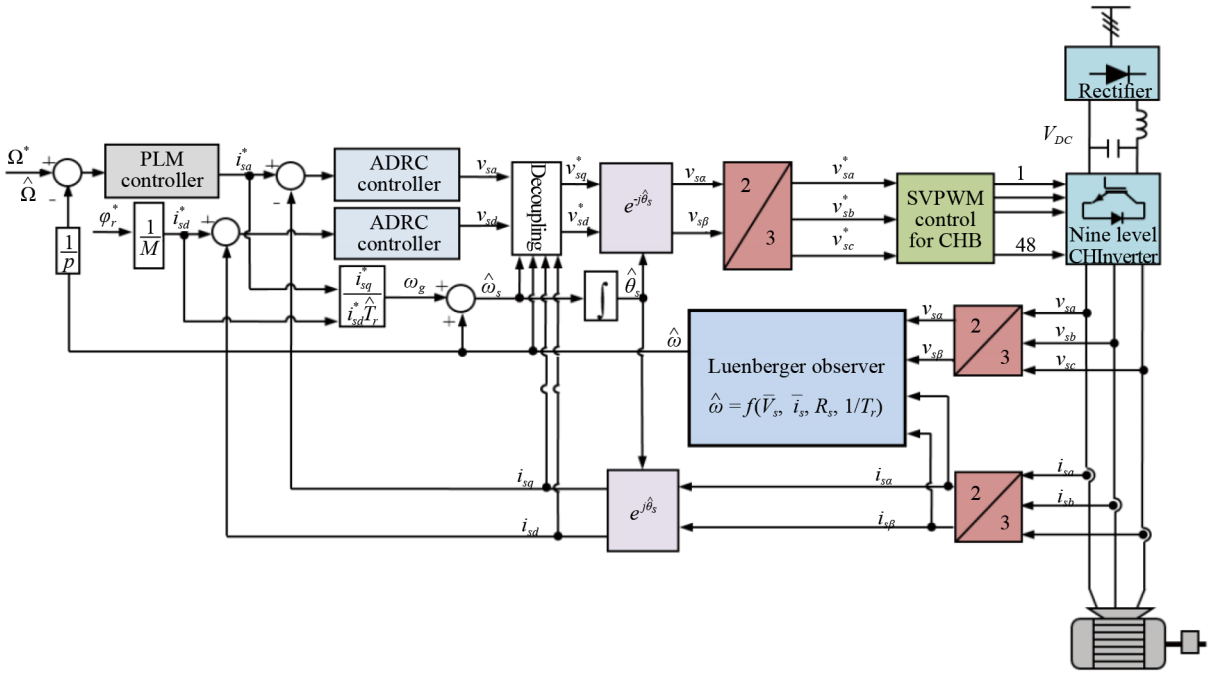

Figure 7. System proposed for a sensor-less induction machine powered by a nine-level converter by combining a PLM control and two ADRC controls

7. Simulation results

To assess the performance and robustness of the control strategies (Poisson Laguerre model, ADRC, and PI), the machine model and its vector control are simulated using Matlab/Simulink. In this paper, the studied machine is powered by a nine-level voltage inverter. In this section, two tests are simulated. While the first test is devoted to illustrating the response of the machine during the variation of the load torque, the second test is meant to test the robustness (variations of parameters). In simulation tests, the predictive control based on Laguerre Poisson models is compared to two controls (ADRC and the classical PI approach).

7.1 *Choice of PLM control parameters*

To assess the performance of predictive control based on PL models, the following test is performed on the variation of the speed: the reference speed value is kept at 0 rad/s from 0 to 1 second, then increased to 100 rad/s from 1 to 4 seconds. Figure 8 illustrates a comparison among the three proposed cases (case 1, case 2, and case 3) for values different from λ The adjustment coefficients for the PLM used were:

• Case 1 (PLM1): $\lambda = 1.4,\ n = 3,\ g_1 = -1.8994,\ g_2 = -0.0601,\ g_3 = -0.0333$.
• Case 2 (PLM2): $\lambda = 1.2,\ n = 3,\ g_1 = -1.3054,\ g_2 = 0.1408,\ g_3 = 0.1980$.
• Case 3 (PLM3): $\lambda = 1.6,\ n = 3,\ g_1 = -2.2084,\ g_2 = -0.0698,\ g_3 = -0.0388$.

The parameters of induction motor are: $L_s = 0.973$ H, $L_r = 0.3558$ H, $R_s = 6.8\ \Omega$, $Rr = 5.4\ \Omega$; $M = 0.39$ H, $p = 2$, $J = 0.02$ kg·m^2; $K_f = 0.0025$ N·m·s/rad, $P = 1$ kw. The flux rotor reference is maintained at 0.89 Wb.

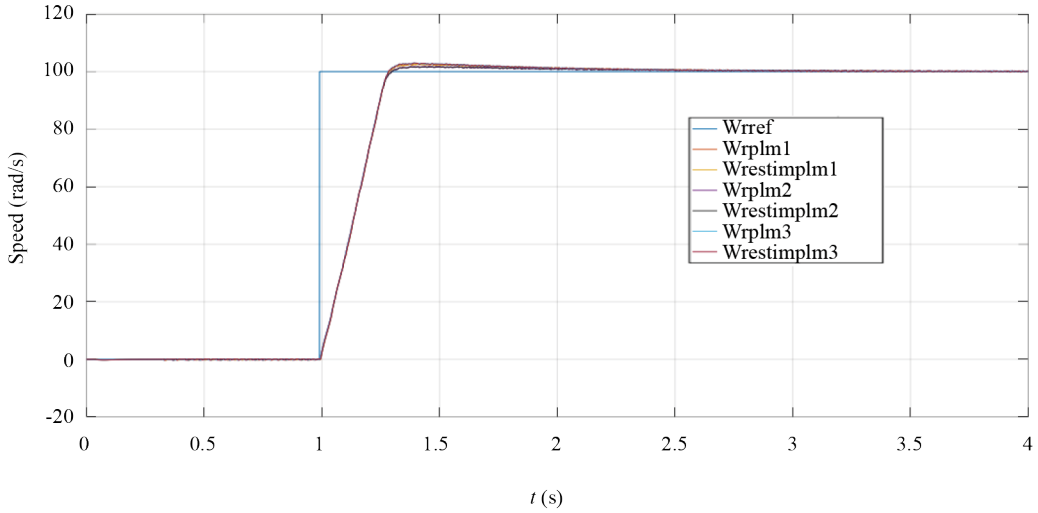

Figure 8. Evolution of the mechanical speed in the three cases (PLM1, PLM2, and PLM3)

The speed forms have been zoomed on the time interval [1.2 s, 3 s] Figure 9. Note that the mechanical speed curve obtained with the second case parameters is good. The speed curve is almost similar for all three cases. So we use this PLM2 case to compare it with the ADRC and PI command.

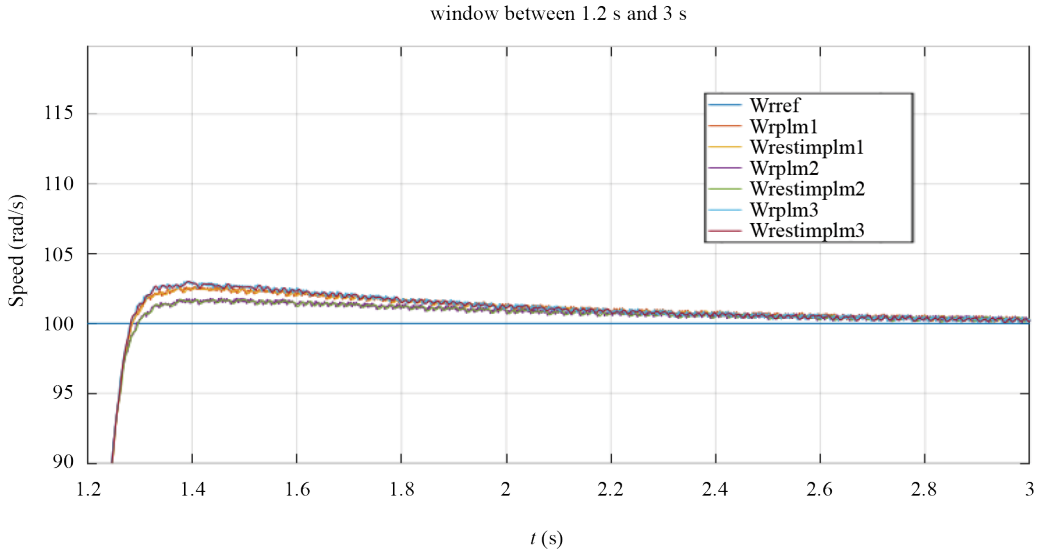

Figure 9. Evolution of mechanical speed for the three cases (PLM1, PLM2, and PLM3) zoomed in from 1.2 to 3 seconds

7.2 *Load torque variation test and speed variation test*

In this test scenario, the reference speed remains constant at 0 rad/s from 0 to 1 second, then ramps up to 100 rad/s from 1 second to 6 seconds, and subsequently decreases to -100 rad/s from 6 seconds to 10 seconds. Concurrently, the load torque is maintained at 0 N·m from 0 seconds to 4 seconds, increases to 5 N·m from 4 seconds to 8 seconds, and finally decreases to -1 N·m from 8 seconds to 10 seconds. The ADRC corrector parameters used to compare with the PLM command are: ADRC for, $Ce = f(\omega) : K_{pw} = 6.6667$, $b_0 = 50$. ADRC control for $V_{sq} = f(i_{sq}) : K_{piq} = 363.6364$, $b_{iq} = 24.0964$. ADRC control for $V_{sd} = f(i_{sd}) : b_{id} = 24.0964$, $K_{pid} = 363.6364$. The adjustment coefficients for the PLM used were Case 2: $\lambda = 1.2$, $n = 3$, $g_1 = -1.3054$, $g_2 = 0.1408$, $g_3 = -0.1980$. The PI corrector parameters used to compare with the PLM command are: $K_p = 0.2397$, $K_i = 0.7201$.

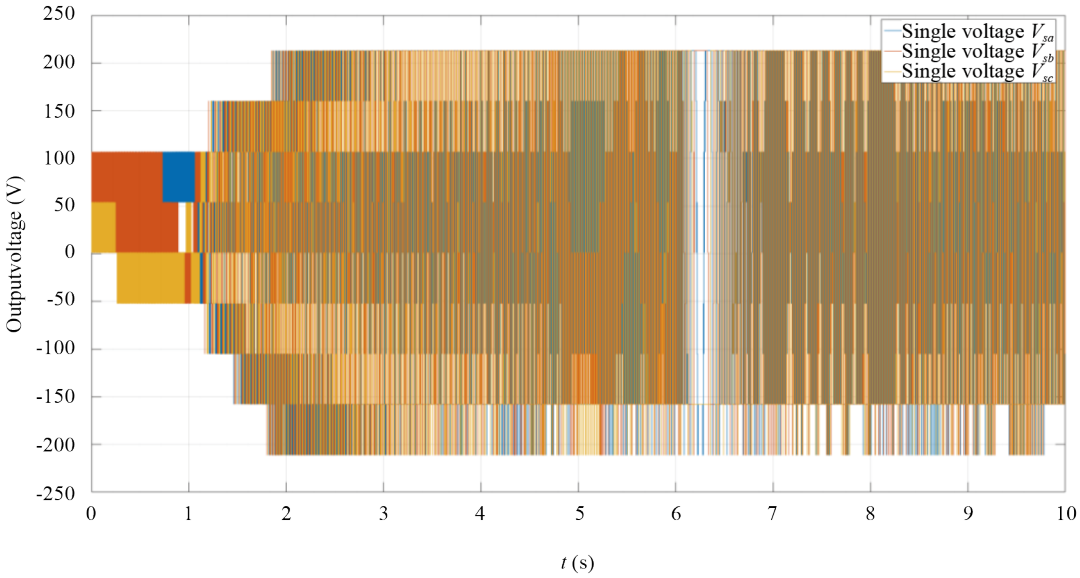

Figure 10. Phase voltages obtained at the output of the nine-level converter

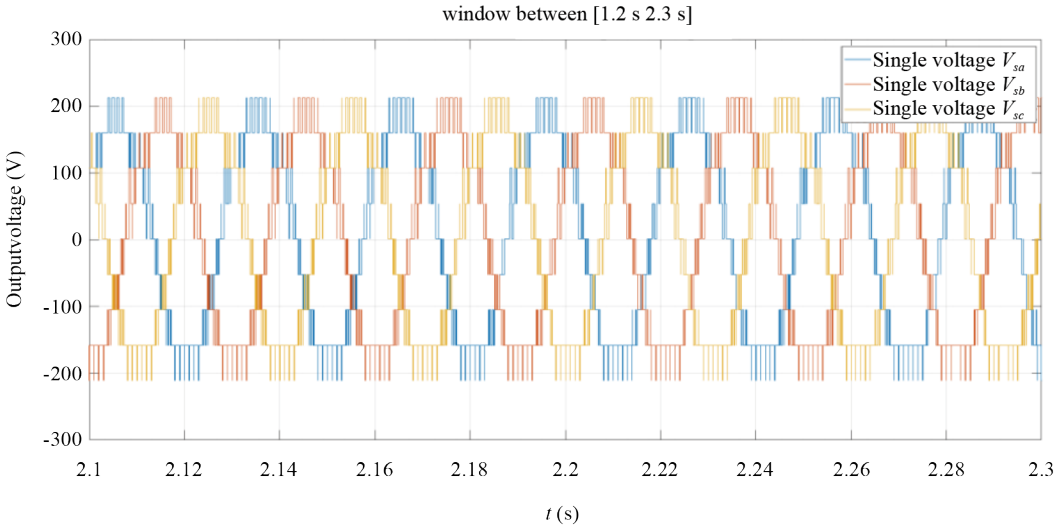

Figure 11. Phase voltages were obtained at the output of the nine-level converter (zoomed in from 2.1 seconds to 2.3 seconds)

The mechanical speed is estimated using the Luenberger observer technique. Initially, the simulation result (Figure 10) shows the output voltages applied to the machine. It is worth noting that the output voltage has 9 levels with a THD value of 13.89%. This value is significantly lower compared to what is achieved with a 3 or 5-level converter. By reducing the THD, the voltage becomes cleaner with fewer undesirable harmonics. This results in a more stable and consistent voltage, reducing electrical interferences and enhancing the performance of electrical equipment connected to the grid. The voltage forms have been zoomed on the time interval [2.1 s, 2.3 s] (Figure 11). It is noticed that the closed-loop system works correctly since the simple voltages applied to the machine have nine levels.

The stator currents are illustrated in Figure 12 while the same currents have been zoomed on the interval [5 s 5.5 s]. We note the trend of the curves of the currents towards sinusoidal form (Figure 13).

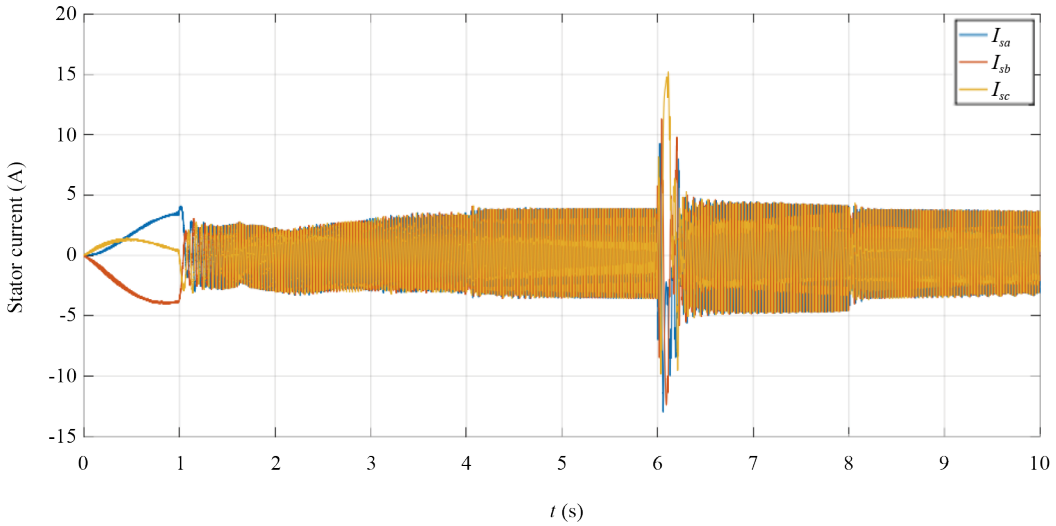

Figure 12. The stator currents obtained at the output of the induction motor

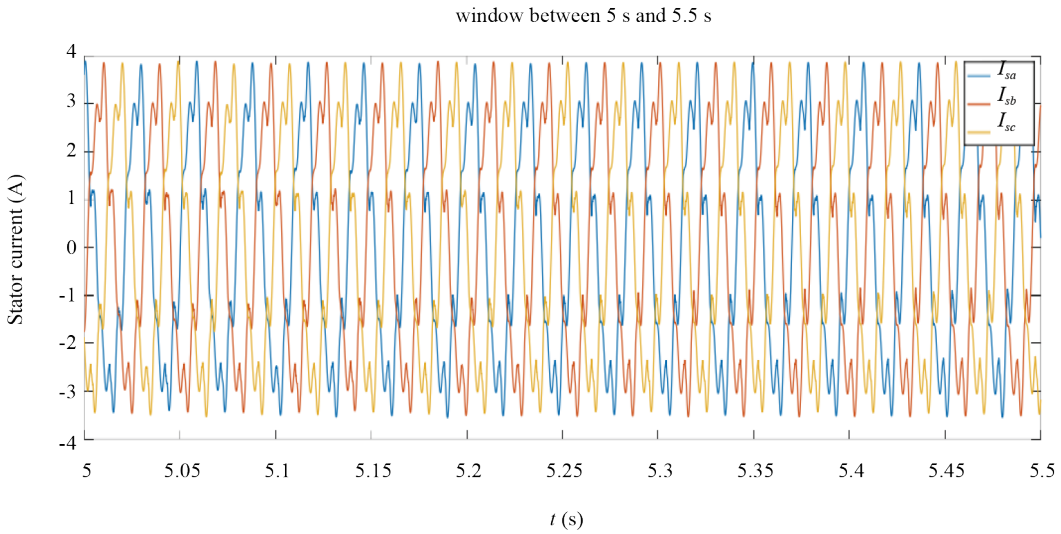

Figure 13. The stator currents obtained at the output of the induction motor (zoomed between 1.2 s and 2 s)

Figure 14 shows the rotor speed curve (actual and estimated) for three systems (PLM, ADRC, PI). In this figure, the speed response with ADRC follows the reference speed is faster than that obtained by the PLM and PI commands. Indeed, by observing the evolution of the mechanical speed waveform, we note that a steady state is reached after 0.25 seconds for the ADRC control, after 0.45 seconds for the PLM control, while for the PI control, a steady state is achieved after 0.65 seconds.

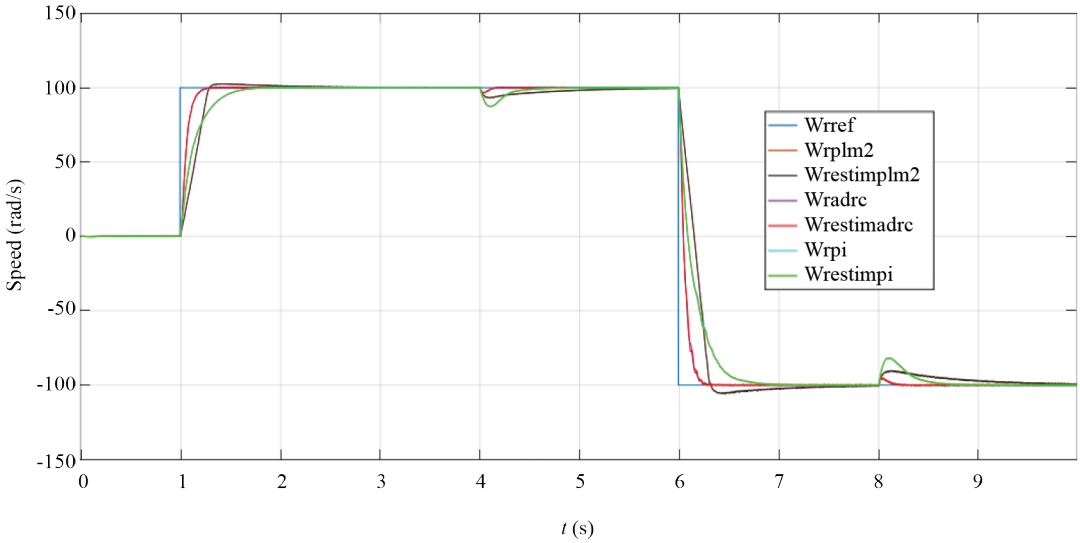

Figure 14. Evolution of the actual and estimated mechanical speed in the three cases (PLM2, ADRC, and PI)

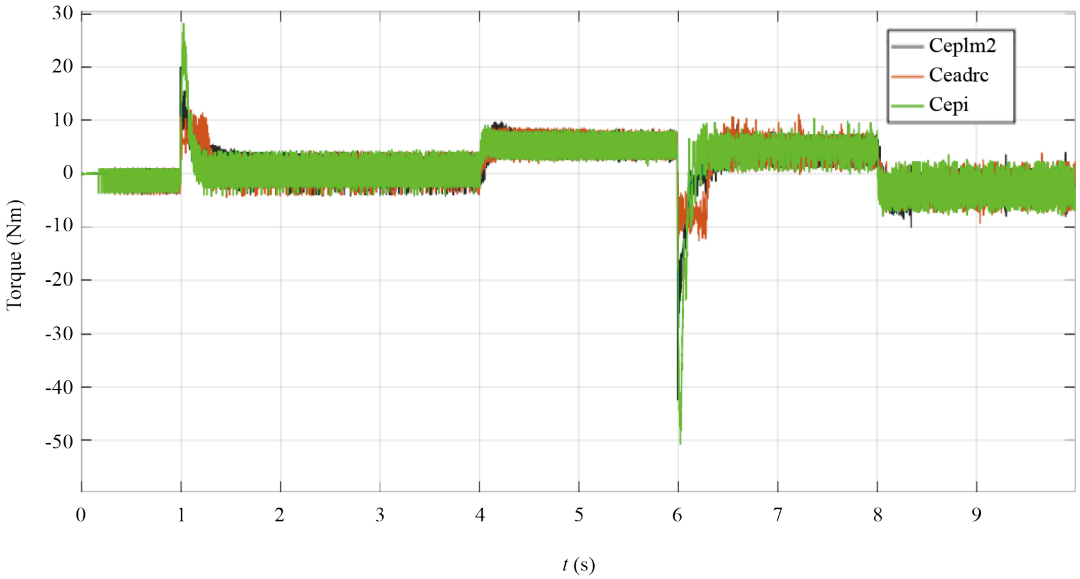

Figure 15. Evolution of the electromagnetic torque in the three cases (PLM2, ADRC, and PI)

Figure 15 clearly demonstrates that the torque performance of the system with ADRC is better than that obtained using PLM2 and PI controllers. The amplitude of the torque during the speed variation is well limited with the ADRC control. Similarly, the load torque variation is quickly taken by the ADRC control in comparison with that of PLM and

PI. In all three cases, electromagnetic torque interferences are significantly reduced due to the decrease in Total Harmonic Distortion (THD) of the asynchronous machine's supply voltage. This helps maintain the smooth and reliable operation of the machine.

The various findings drawn from the results are illustrated in Table 2. This table clearly shows the impact of the three controls: PI, ADRC, and PLM, on the proposed system, particularly on the evolution of the mechanical speed of the asynchronous machine.

Table 2. Comparison of the three controls PLM, ADRC, and PI in response to variations in speed and torque

Type of control	Impact on the system due to step changes in rotational speed and load torque
PI	- It is simple to implement and effective for stable systems with predictable disturbances. However, it may not handle varying or complex disturbances well without tuning adjustments. - PI control can ensure stable speed rise, but it may require fine-tuning of parameters to prevent oscillations or overshoot. - The response time under PI control can be relatively fast for well-tuned and stable systems, but it may be limited by the need to manually adjust proportional and integral parameters for different operating conditions. - PI control can maintain effective regulation of electromagnetic torque provided that the parameters are properly tuned for the specific characteristics of the motor.
PLM	- By employing predictive models and adaptive strategies, PLM optimizes speed ramp-up by continuously adjusting controls to minimize errors and maximize motor performance. - By utilizing adaptive models, PLM can adjust its control strategies to optimize electromagnetic torque based on operational conditions and load requirements. - PLM provides a fast response time by using predictive models to anticipate system variations and adjust control actions accordingly.
ADRC	- ADRC is effective in handling external and internal disturbances affecting the speed of asynchronous motors, offering a quick and stable response even under varying load conditions or disturbances. - By actively rejecting disturbances, ADRC can maintain more stable electromagnetic torque in the presence of load variations or changing dynamic conditions. - ADRC typically has a fast response time because it can quickly estimate and react to disturbances.

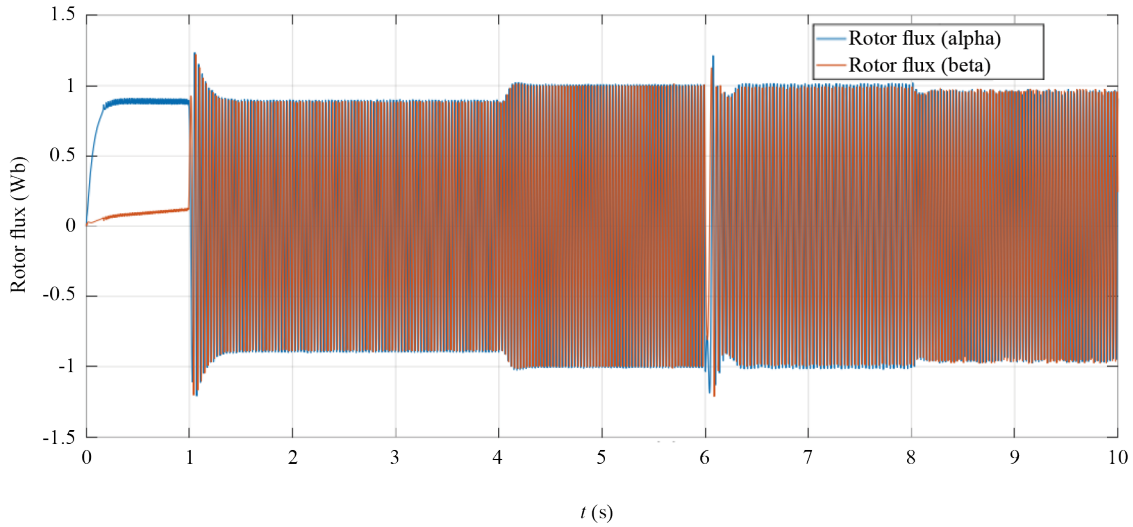

Figure 16. The curves of the rotor flux along axes α and β

7.3 *Validity test of the Luenberger observer*

Under the same conditions of section 7.2, Figure 16 shows the observed state vector and in particular the two flux (rotor flux on axis α, rotor flux on axis β). The flux is zoomed on the interval [2 s 2.5 s]. Figure 17 shows that the waveform of the flow along the axes is sinusoidal.

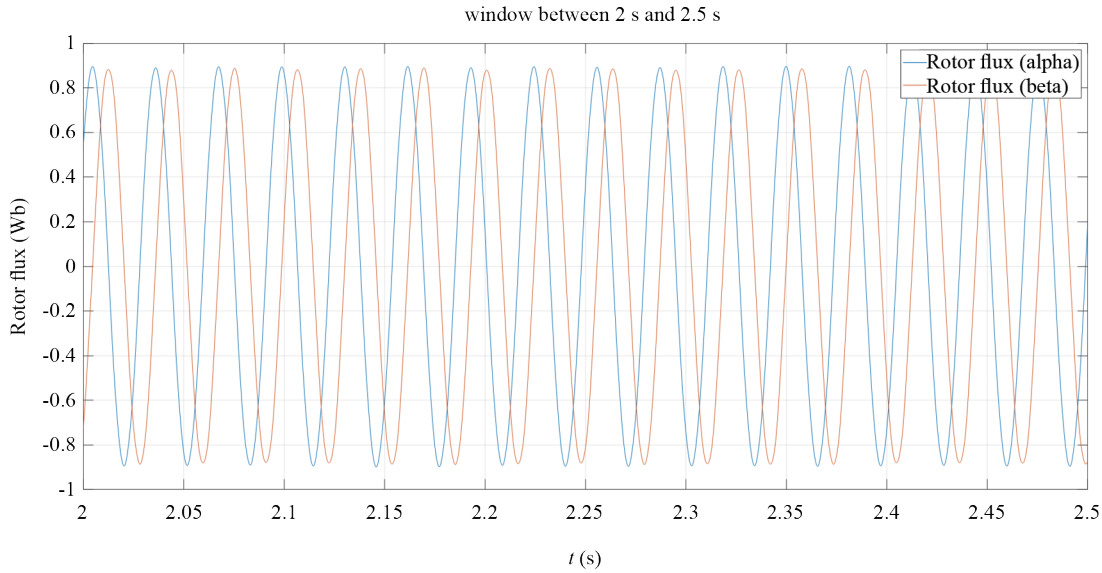

Figure 17. The curves of the rotor flux along axes α and β (zoomed between 1.2 s and 2 s)

7.4 *Robustness test: IM operation with rotor resistance variation and moment of inertia variation*

To test the robustness of the proposed system, some machine parameters (rotor resistance R_r and moment of inertia J) are modified. Indeed, these parameters may vary due to internal disturbances or other external physical phenomena. The system is tested by simulation in the following case: The parametric variations are 50% of the resistance of the rotor R_r at 5.5 s and 50% of the moment of inertia J at 5.5 s. After the variations that affected the parameters (R_r and J) at $t = 5.5$ s. It is observed that variations in these parameters do not impact the stability of the system. Figure 18 illustrates the evolution of the mechanical speed (actual and estimated). Based on the evolution of the mechanical speed waveform, at $t = 5.5$ s (the onset of internal and external parameter variations), and at $t = 6$ s (when the rotation direction is reversed), we observe that steady-state is reached more quickly with the ADRC control compared to PLM and PI controls. Furthermore, comparing the results between Figure 14 (without internal parameter variations) and Figure 18 (with internal and external parameter variations), we notice a slight overshoot in all three-speed curves (ADRC, PLM, PI) in Figure 18. The overshoot observed with ADRC is slightly lower than that with PLM and PI controls. Figure 19 illustrates the evolution of the electromagnetic torque. Despite the parametric variations at $t = 5.5$ s, we find that in all three cases (PLM, ADRC, and PI) the electromagnetic torque was not affected. However, the ADRC-based system is better than the PLM and PI based system.

The conclusions drawn from the results are illustrated in Table 3, clearly demonstrating the impact of the three controls-PI, ADRC, and PLM-on the proposed system in response to variations in internal and external parameters.

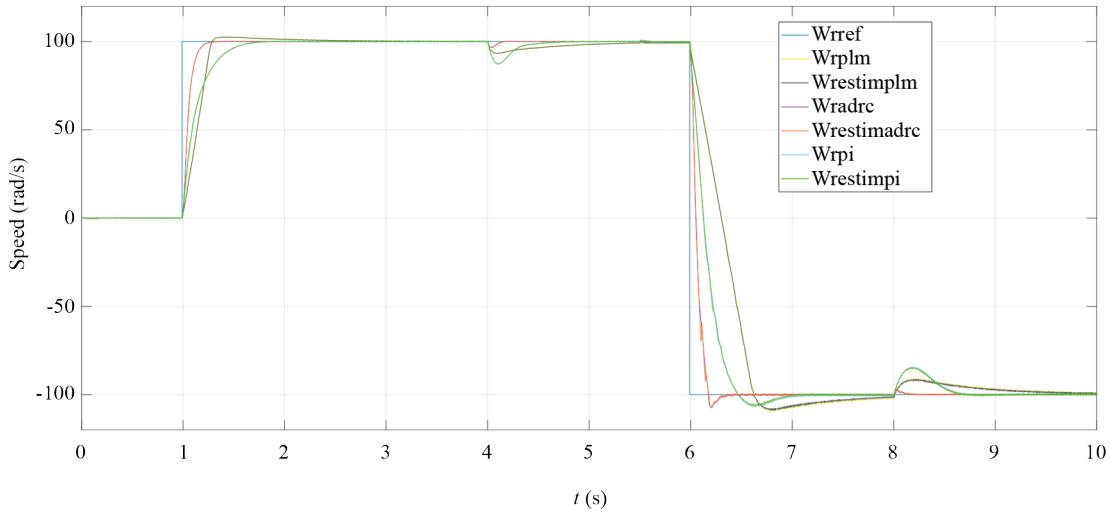

Figure 18. Evolution of the actual and estimated mechanical speed (PLM, ADRC, and PI)

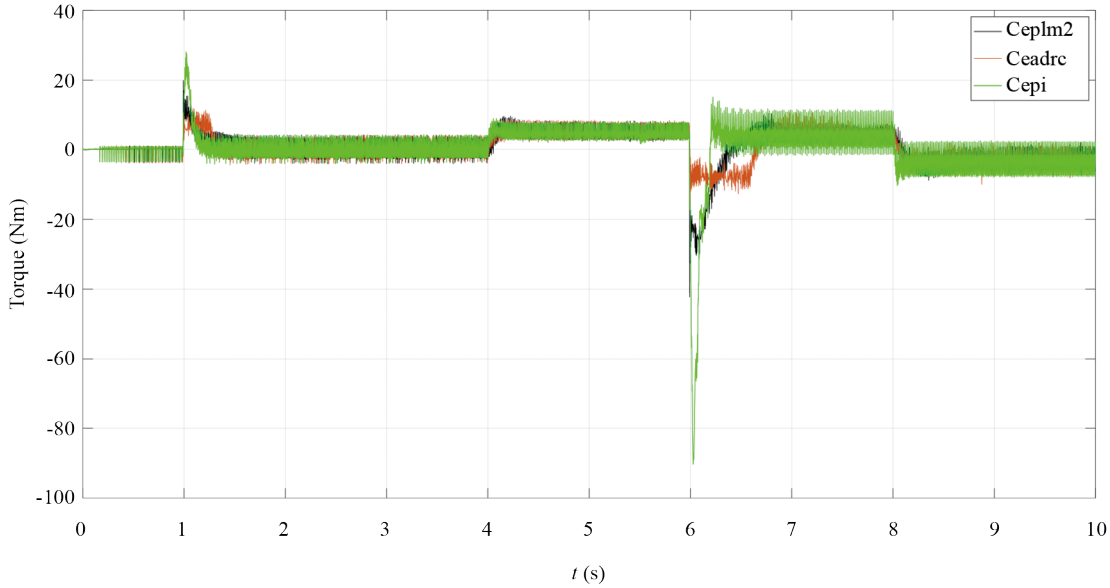

Figure 19. Simulated electromagnetic torque curves (PLM, ADRC, and PI)

Table 3. Comparison of the three controls PLM, ADRC, and PI in response to variations in internal and external parameters

Type of control	Impact on the system due to changes in internal and external parameters
PI	- Less effective in directly managing resistance variations as they rely on simpler models and may require manual adjustments to compensate for parameter changes.
PLM	- May require more frequent parameter adjustments to maintain motor performance when the moment of inertia changes.
ADRC	- Generally capable of adapting and rejecting the effects of resistance variations due to its ability to estimate and actively compensate for disturbances. - Can more effectively adjust the control to respond to changes in the moment of inertia using advanced prediction and estimation techniques.

8. Conclusion

In this paper, an APC derived from PLM to improve the dynamic performance of a sensor-less induction motor was developed. The machine whose field is indirectly oriented was powered by a nine-level CHB inverter using SVPWM techniques. PLM control performance was compared to ADRC and PI controls. The results demonstrate a good dynamic performance of the proposed solutions. According to the simulation results, the system based on the ADRC control has a fast response time and accurate output. Indeed, we observed that the closed-loop system using ADRC is 1.8 times faster than the one using PLM, and 2.6 times faster than the one using PI in terms of response time. We also found that the ADRC control provides greater accuracy compared to the PLM and PI controls. With ADRC control, the dynamics of the system quickly converges to the stationary state. During simulations, we noted that ADRC parameters can be adjusted quickly to improve the accuracy of setpoint tracking. The curves of the mechanical quantities confirm that the system with ADRC surpasses the conventional control based on PLM and PI. The Cascade H-Bridge (CHB) Inverter structure was introduced, increasing the output voltage level to nine levels. In addition, the THD was significantly reduced by a factor of 3.16 compared to the conventional SVPWM level 3 control. Finally, from these results, it can be concluded that ADRC is often preferable in environments where operating conditions are variable and quick responses to disturbances are crucial. PI and PLM are simpler and less computationally intensive but may require more frequent monitoring and adjustments to maintain motor performance in the face of parameter changes such as resistance and inertia. In the future, it is planned to explore the use of artificial intelligence techniques, such as neural networks, to implement the nine-level SVPWM algorithm as well as the three control methods in an experimental setup. Our ambition is to implement these controls in an electric car as well as in a helicopter.

Conflict of interest

The authors declare no conflict of interest

References

[1] Casadei D, Profumo F, Serra G, Tani A. FOC and DTC: two viable schemes for induction motors torque control. *IEEE Transactions on Power Electronics*. 2002; 17(5): 779-787.

[2] Miloudi A, Alradadi EA, Draou A. A new control strategy of direct torque fuzzy control of a PWM inverter fed induction motor drive. In *2006 IEEE International Symposium on Industrial Electronics*. Montreal, QC, Canada: IEEE; 2006. p.2535-2540.

[3] Rodriguez J, Lai JS, Peng FZ. Multilevel inverters: a survey of topologies, controls, and applications. *IEEE Transactions on Industrial Electronics*. 2002; 49(4): 724-738.

[4] António-Ferreira A, Collados-Rodríguez C, Gomis-Bellmunt O. Modulation techniques applied to medium voltage modular multilevel converters for renewable energy integration: A review. *Electric Power Systems Research*. 2018; 155: 21-39. Available from: https://doi.org/10.1016/j.epsr.2017.08.015.

[5] Narendra V, Dr Pramod S. Comparison of 9-level cascaded multilevel inverter using multicarrier pulse width modulation techniques. *International Research Journal of Engineering and Technology*. 2021; 8(3): 511-515.

[6] Kim JK, Ko JS, Lee JH, Lee YK. Rotor flux and rotor resistance estimation using extended luenberger-sliding mode observer (ELSMO) for three phase induction motor control. *Canadian Journal of Electrical and Computer Engineering*. 2017; 40(3): 181-188. Available from: https://doi.org/10.1109/CJECE.2017.2682259.

[7] Busireddy HK, Lokhande MM, Karasani RR, Borghate VB. A modified space vector PWM approach for nine-level cascaded H-bridge inverter. *Arabian Journal for Science and Engineering*. 2018; 44(3): 2131-2149. Available from: https://doi.org/10.1007/s13369-018-3363-3.

[8] Oukassi A, Elbourhichi S. Sensorless indirect control of induction motor fed by a multi-level inverter with consideration of variation in rotor and stator resistances. In *2020 7th International Conference on Electrical and Electronics Engineering (ICEEE)*. Antalya, Turkey: IEEE; 2020. p.142-149.

[9] Kandoussi Z, Boulghasoul Z, Elbacha A, Tajer A. Sensorless control of induction motor drives using an improved MRAS observer. *Journal of Electrical Engineering & Technology*. 2017; 12(4): 1456-1470.

[10] Aydeniz MG, Şenola I. Luenberger-sliding mode observer with rotor time constant parameter estimation in induction motor drives. *Turkish Journal of Electrical Engineering & Computer Sciences*. 2011; 19(6): 901-912. Available from: https://doi.org/10.3906/elk-1004-4.

[11] Han J. From PID to active disturbance rejection control. *IEEE Transactions on Industrial Electronics*. 2009; 56(3): 900-906. Available from: https://doi.org/10.1109/TIE.2008.2011621.

[12] Saadatmand M, Mozafari B, Gharehpetian B Gevork, Soleymani S. Optimal fractional-order PID controller of inverter-based power plants for power systems LFO damping. *Turkish Journal of Electrical Engineering & Computer Sciences*. 2020; 28(1): 485-499.

[13] El Bourhichi S, Oukassi A, El Bahir L, El Adnani M. Active disturbance rejection control for a five-level cascaded h-bridge inverter Fed induction motor sensorless field-oriented. *Mathematical Problems in Engineering*. 2021; 5(8): 1-13. Available from: https://doi.org/10.1155/2021/9925072.

[14] Tamim TM, Li S, Wu J. Multi-level model predictive controller with satisfactory optimization for multi-level converters. *Simulation Modelling Practice and Theory*. 2019; 92: 1-16. Available from: https://doi.org/10.1016/j.simpat.2018.11.003.

[15] Cortés P, Wilson A, Kouro S, Rodriguez J, Abu-Rub H. Model predictive control of multilevel cascaded H-bridge inverters. *IEEE Transactions on Industrial Electronics*. 2010; 57(8): 2691-2699. Available from: https://doi.org/10.1109/TIE.2010.2041733.

[16] Kim I, Chan R, Kwak S. Model predictive control method for CHB multi-level inverter with reduced calculation complexity and fast dynamics. *IET Electric Power Applications*. 2017; 11(5): 784-792. Available from: https://doi.org/10.1049/iet-epa.2016.0330.

[17] Lahooti Eshkevari A, Arasteh M. Model-predictive Direct Power Control of three-phase three-level NPC PWM rectifier. In *2017 8th Power Electronics, Drive Systems Technologies Conference (PEDSTC)*. Mashhad, Iran: IEEE; 2017. p.78-83.

[18] Maheswari KT, Bharanikumar R, Arjun V, Amrish R, Bhuvanesh M. A comprehensive review on cascaded H-bridge multilevel inverter for medium voltage high power applications. *Materials Today: Proceedings*. 2021; 45(2): 2666-2670. Available from: https://doi.org/10.1016/j.matpr.2020.11.519.

[19] Chitra S, Valluvan KR. Design and implementation of cascaded H-Bridge multilevel inverter using FPGA with multiple carrier phase disposition modulation scheme. *Microprocessors and Microsystems*. 2020; 76: 103108. Available from: https://doi.org/10.1016/j.micpro.2020.103108.

[20] Patthi S, Murali Krishna VB, Reddy L, Arandhakar S. Photovoltaic string fault optimization using multi-layer neural network technique. *Results in Engineering*. 2024; 22: 102299. Available from: https://doi.org/10.1016/j.rineng.2024.102299.

[21] Bourhichi SE, Oukassi A, Bahir LE, Adnani ME. Indirect vector control of induction motor based on five-level inverter cascaded H-bridge using space vector modulation. In *2021 8th International Conference on Electrical and Electronics Engineering (ICEEE)*. Antalya, Turkey: IEEE; 2021. p.112-116.

[22] Ahmed I, Borghate VB. Simplified space vector modulation technique for seven-level cascaded H-bridge inverte. *IET Power Electronics*. 2014; 7(3): 604-613. Available from: https://doi.org/10.1049/iet-pel.2013.0135.

[23] Boulghasoul Z, Kandoussi Z, Elbacha A, Tajer A. Fuzzy improvement on luenberger observer based induction motor parameters estimation for high performances sensorless drive. *Journal of Electrical Engineering & Technology*. 2020; 15(2): 2197. Available from: https://doi.org/10.1007/s42835-020-00495-6.

[24] Kubota H, Matsuse K. Speed sensorless field-oriented control of induction motor with rotor resistance adaptation. *IEEE Transactions on Industry Applications*. 1994; 30(5): 1219-1224. Available from: https://doi.org/10.1109/28.315232.

[25] You J, Wu W, Wang Y. An adaptive luenberger observer for speed-sensorless estimation of induction machines. In *2018 Annual American Control Conference (ACC)*. Milwaukee, WI, USA: IEEE; 2018. p.307-312. Available from: https://doi.org/10.23919/ACC.2018.8431006.

[26] Vaclavek P, Blaha P. Lyapunov-function-based flux and speed observer for AC induction motor sensorless control and parameters estimation. *IEEE Transactions on Industrial Electronics*. 2006; 53(1): 138-145. Available from: https://doi.org/10.1109/TIE.2005.862305.

[27] Kubota H, Matsuse K, Nakano T. DSP-based speed adaptive flux observer of induction motor. *IEEE Transactions on Industry Applications*. 1993; 29(2): 344-348. Available from: https://doi.org/10.1109/28.216542.

[28] Blaschke F. The principles of field orientation as applied to the new tran vector closed loop control system for rotating field machines. *Siemens Review*. 1972; 24: 217-220.

[29] El Bahir L. An adaptive luenberger observer for speed-sensorless estimation of induction machines. In *IMACS-IEEE CSCC 99*. Athens, Greece: IMACS-IEEE; 1999. p.243-249.

[30] Abd-Elhameed W, Al-Sady A. Some orthogonal combinations of legendre polynomials. *Contemporary Mathematics*. 2004; 5(2): 1522-1551. Available from: https://doi.org/10.37256/cm.5220243525.

[31] El Bahir L. Continuous-time Predictive Control based on Poisson-Laguerre models. In *Proceedings of the 38th Conference on Decision Control Phoenix 1999*. Arizona, USA: IEEE; 1999. p.4601-4606.

[32] Boulghasoul Z, El Bahir L, Elbacha A, Elwarraki E. Adaptive-predictive controller based on continuous-time laguerre-poisson models for induction motor speed control improvement. *Journal of Electrical Engineering and Technology*. 2014; 9(3): 908-925. Available from: https://doi.org/10.5370/JEET.2014.9.3.908.

[33] Han J. From PID to active disturbance rejection control. *IEEE Transactions on Industrial Electronics*. 2009; 56(3): 900-906. Available from: https://doi.org/10.1109/TIE.2008.2011621.

[34] Huang Y, Xue W. Active disturbance rejection control: Methodology and theoretical analysis. *ISA Transactions*. 2014; 53(4): 963-976. Available from: https://doi.org/10.1016/j.isatra.2014.03.003.